buildings

MDPI

Article

Effects of Openings and Axial Load Ratio on the Lateral Capacity of Steel-Fiber-Reinforced Concrete Shear Walls

Zhou Lin [1], Hongmei Zhang [1,*], Giorgio Monti [1,2] and Chiara Castoro [3]

[1] College of Civil Engineering and Architecture, Zhejiang University, Hangzhou 310058, China
[2] Department of Structural Engineering and Geotechnics, Sapienza University of Rome, 00197 Rome, Italy
[3] Department of Civil, Construction-Architectural and Environmental Engineering, University of L'Aquila, 67100 L'Aquila, Italy
* Correspondence: zhanghongmei@zju.edu.cn

Abstract: Shear walls are commonly adopted as main structural members to resist vertical and lateral forces, thanks to their high load capacity and high lateral stiffness. However, their lateral capacity can be impaired in the presence of openings, which can reduce their lateral load capacity and stiffness. A possible solution is to cast shear walls using steel-fiber-reinforced concrete (SFRC), which effectively improves the deformation capacity of shear walls. However, few studies deal with the performance of such SFRC shear walls in the presence of openings. Moreover, the effect of different axial load ratios (ALR) is still not fully known. To study these essential parameters, a detailed Finite Element model has been implemented in ABAQUS. Having validated its accuracy against experimental tests on four SFRC shear walls, with and without openings, it has been subsequently used in a parametric study to analyze the effects of different ALRs, of different opening configurations, and of different reinforcement ratios. It is shown that door openings have a more detrimental effect on the lateral load capacity than window openings and that higher ALR values switch the prevailing failure mechanism from flexural to shear, thus reducing both ductility and deformation capacity.

Keywords: steel-fiber-reinforced concrete; shear wall; lateral capacity; openings; axial load ratio; numerical analysis

Citation: Lin, Z.; Zhang, H.; Monti, G.; Castoro, C. Effects of Openings and Axial Load Ratio on the Lateral Capacity of Steel-Fiber-Reinforced Concrete Shear Walls. *Buildings* **2022**, *12*, 2032. https://doi.org/10.3390/buildings12112032

Academic Editor: Hossam El-Din Sallam

Received: 8 October 2022
Accepted: 10 November 2022
Published: 21 November 2022

1. Introduction

Shear walls are the main structural members to resist vertical and lateral forces in high-rise buildings in seismic zones, thanks to their high vertical load capacity and high lateral stiffness and resistance. An important parameter affecting the lateral load and deformation capacity of shear walls is the axial load ratio (ALR) [1–4]. Shear walls at the lower stories of high-rise buildings have relatively high axial load ratio (ALR), which may induce significant damage when combined with horizontal earthquake forces. Particularly, concrete at the bottom corners can be easily crushed under seismic conditions [5]. Typically, shear walls are endowed with doors and windows, which often cause stress concentration around the openings [6]. Moreover, shear walls show a brittle behavior, mainly due to the low tensile strength of concrete. In this respect, several studies [4,7–10] demonstrate that the addition of steel fibers can improve the tensile strength of concrete, and show that shear walls cast using steel-fiber-reinforced concrete (SFRC) exhibit a better deformation capacity. While, in general terms, the adoption of SFRC may be beneficial for the overall behavior of shear walls, it is still unclear how this can be affected, both by the presence of openings and by high ALR.

Useful insight on these issues can be gained from the literature studies referring to different opening configurations. For example, Zhang et al. [11] conducted experimental and numerical studies on shear walls, proving that openings have significant influence on their performance under lateral loads. Popescu et al. [12] reported three experimental programs on RC shear walls with different opening configurations, which indicate that the

presence of 25–50% openings produces 36–50% degradation on lateral bearing capacity, respectively. Experimental tests on four slender shear walls by Massone et al. [13] indicate that openings with 15–30% of the wall length and with 11–22% of the wall height do not significantly affect the lateral load capacity of slender walls (in those tests, the overall walls size was 2650 mm high, 900 mm wide, and 150 mm thick). Other studies investigated the influence, under cyclic loading, of openings size and position and shear wall height-to-width ratio. For example, an experimental study by Wang et al. [14] shows that, in case of eccentric opening locations, the load capacity depends on the loading direction. Hosseini et al. [6] investigated the structural performance of RC shear walls with different eccentric openings, showing that differences in the load capacity occurred under both push and pull loading directions, these differences at peak load being about 2%, 6.2%, and 12.5%, respectively. However, they did not identify possible reasons for these differences, such as the influence of steel fiber and reinforcement ratios. Another parameter having a critical role in the lateral capacity of RC shear walls is ALR. Su et al. [3] investigated the effect of ALR on shear walls and concluded that ALR not only affects failure mode but also rotation ductility, strength degradation, and energy dissipation. Alarcon et al. [2] also found that high ALR has a significant effect on the lateral capacity and failure mode of RC walls. An experimental study on cantilever wall specimens and corresponding numerical analysis by Dashti et al. [15] revealed that the effects of ALR on RC structures are complex because it can easily change the failure mode, e.g., from flexure to shear or flexure–out-of-plane to flexure–concrete crushing, and it highly depends on other parameters such as the shear–span ratio. A wide range of investigations has been carried out concerning the effect of ALR on RC shear walls, but there are few studies on SFRC shear walls with ALR, in view of the improvement of concrete tensile strength by steel fiber, the effect of ALRs on SFRC walls is still not clear.

An overview of these studies is given in Table 1, where it can be observed that there exist a wide range of investigations concerning the effect of both openings and ALR on RC walls, but also that there are relatively few studies dealing with the role of openings in SFRC shear walls under variable ALR. Since SFRC can improve the overall response with respect to traditional concrete, it is essential to perform some studies aimed at clarifying such aspects. This study brings a contribution in filling this research gap. The methodology adopted foresees to set up four finite element (FE) models representing the four SFRC shear walls tested by Huang [16]. Subsequently, after having calibrated these FE models against those experimental results and having assessed their accuracy, the models were modified by changing the openings configuration, the ALR, and the reinforcement ratio, so to explore other situations not considered in the original experimental study.

The main outcomes of this study can be summarized as follows: (1) a practical SFRC constitutive law has been compiled from a series of studies, which can capture the stress–strain relationship of SFRC in compression and in tension, (2) a detailed and accurate FE model has been implemented in ABAQUS, which can be used as a basis for further parametric studies, (3) the main parameters affecting the lateral capacity of SFRC shear walls have been identified, e.g., openings, ALR, and reinforcement ratio, (4) a matrix is proposed to classify failure modes in SFRC shear walls, and (5) a design scheme is proposed, accounting for the presence of window and door openings.

Table 1. Overview of the literature studies on shear walls.

Ref	Concrete Type	Exp	Num	Equ	ALR Computed According to		Openings		
					Equation (20)	Equation (21)	No	Win	Door
[17]	RC			√		√	√		
[18]	RC	√		√	−0.1, 0.3, 0.5	-	√		
[19]	RC	√		√	0.03	0.06	√		
[20]	RC	√		√	0.013, 0.016, 0.013	0.039, 0.049, 0.029	√		
[21]	RC	√		√	0.1, 0.2, 0.3	-	√		
[22]	RC	√	√			0.0	√	√	√
[23]	RC	√			0.15	-	√		
[6]	RC	√				0.0	√		√
[24]	RC	√	√		0.1	-	√	√	
[25]	RC	√			0.08, 0.13	-	√		
[26]	RC	√				0.0		√	
[11]	RC	√		√	0.090, 0.092	-		√	√
[13]	RC	√	√		0.07	-			√
[12]	RC	√				-	√		√
[2]	RC	√			0.15, 0.25, 0.35	-	√		
[4]	RC, SFRC	√		√	-	0.4, 0.6	√		
[27]	RC, SFRC	√		√		0.0	√		
[28]	RC, SFRC	√		√	-	0.3	√		
[29]	SFRC	√		√	0.1	-	√		
[16]	SFRC	√		√		0.0	√	√	√
[30]	SFRHSC	√	√		-	0.2, 0.6, 0.8	√		
[31]	UHPFRC		√			0.0	√		
[32]	UHPFRC	√		√	0.1	-	√		
[33]	UHPFRC	√		√		0.0	√		
[34]	RC			√		√	√		
[35]	RC		√			√	√		
[36]	RC			√		√	√		

RC: Reinforced Concrete, SFRC: Steel-Fiber-Reinforced Concrete, UHPFRC: Ultra-High-Performance-Fiber Reinforced Concrete, SFRHSC: Steel-Fiber-Reinforced High Strength Concrete. Exp: Experimental study, Num: Numerical analysis, Equ: Capacity equations, ALR: Axial Load Ratio, Win: Window, (-) denotes that the corresponding ALR was not considered in the reference.

2. Finite Element Models Used in the Parametric Study

The parametric study presented in the following section has been performed by means of a set of finite element (FE) models, developed in ABAQUS. These models have been chosen to have the same geometry, detailing, and material properties as the specimens of a series of tests conducted by Huang [16]. After some sensitivity analyses, they have been calibrated so to accurately reproduce those experimental results. Once their accuracy has been ascertained, these models have been used in the parametric study to assess the effects of eccentric openings and different ALR values, including a case with eccentric opening and low reinforcement ratio. In this section, details regarding the FE model are given, while the parametric study is presented in the following chapter.

2.1. Tests Conducted by Huang [16]

Huang [16] conducted a series of tests on four different SFRC shear walls, all under ALR = 0. Each specimen consisted of a base beam, a wall, with or without opening, and a top beam. The detailed geometry and reinforcement of the reference specimens are shown in Figure 1, while the material constitutive laws are presented in the following section.

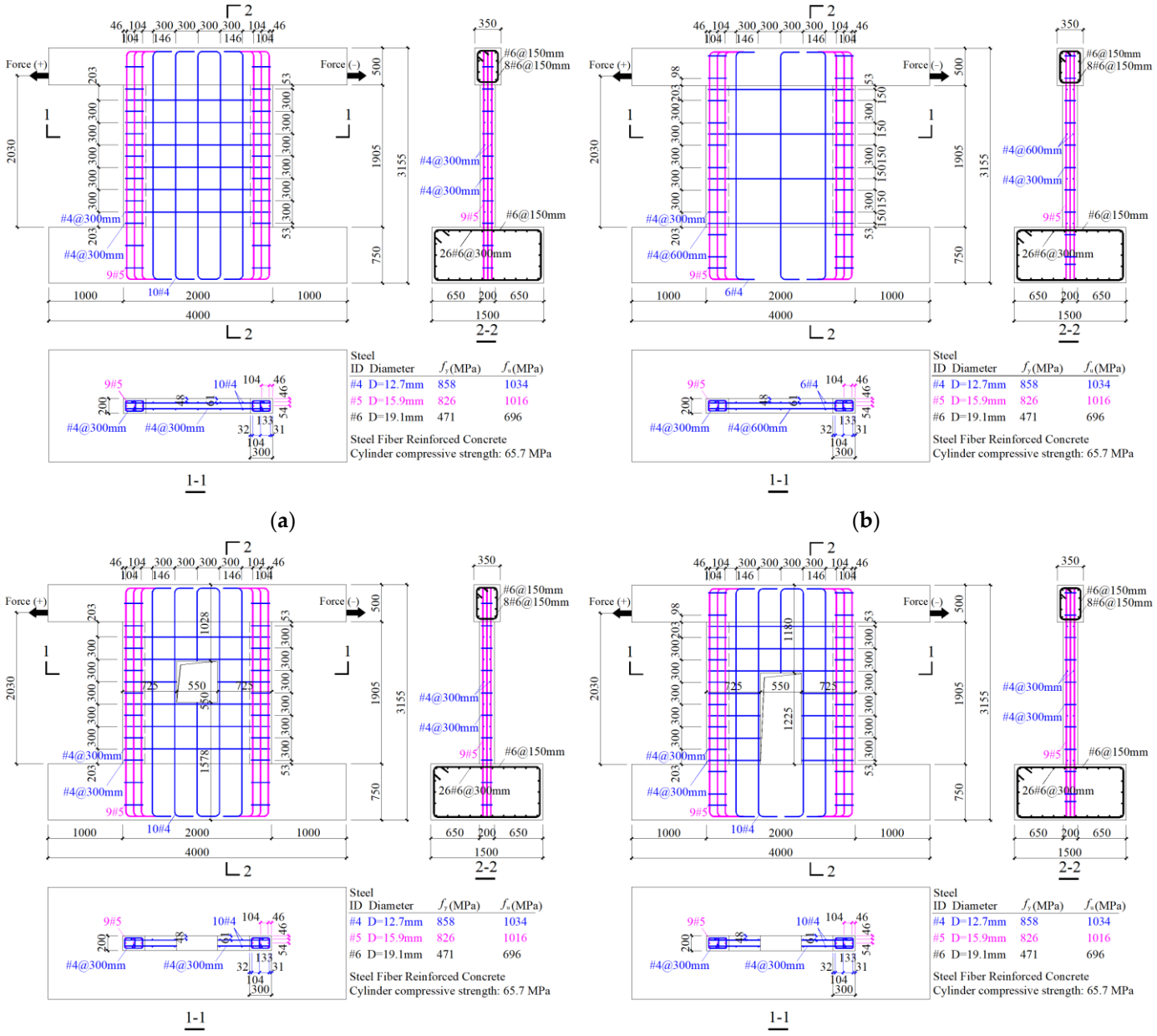

Figure 1. Geometry and reinforcement of the specimens tested by [16]: (**a**) SFW, (**b**) SFW60, (**c**) SFWO, (**d**) SFWCD. These specimens were used to calibrate the FE models.

2.2. SFRC Constitutive Law

2.2.1. Uniaxial Compression Stress-Strain Relationship

Cylindrical compressive strength $f_{c,cyl}$ of SFRC with hooked-end steel fibers can be obtained either directly from 150 × 300 mm cylinder tests or, if 150 × 150 × 150 mm cubic compressive strength f_{cu} is available, from:

$$f_{c,cyl} = \begin{cases} 0.83 f_{cu} & 30 \text{ MPa} \leq f_{cu} \leq 50 \text{ MPa} \\ f_{cu} - 10 & 50 \text{ MPa} < f_{cu} \leq 90 \text{ MPa} \end{cases} \quad (1)$$

Some parameters describing the SFRC used in this study are listed in Table 2.

Table 2. Parameters of the SFRC used in this study.

Cylindrical compressive strength, $f_{c,cyl}$	65.7 MPa
Volume fraction of the fiber, V_f	1.5%
Length of the fiber, l_f	30 mm
Diameter of the fiber, d_f	0.38 mm
Tensile strength of the fiber	2300 MPa

From these parameters, the fiber reinforcement index is defined as:

$$RI = V_f \frac{l_f}{d_f} \tag{2}$$

Extensive experimental and analytical studies on SFRC have been carried out [8,9,37–43]. In [9] a comparison study is reported of different stress-strain equations proposed in the literature, validated versus experimental stress-strain curves. It was found that the one proposed in [38] shows a good agreement and is therefore adopted here, with a slight modification of the elastic stage, as follows:

$$\varepsilon_0 = (0.0003RI + 0.0018) f_{c,cyl}^{0.12} \tag{3}$$

$$E_c = (-367RI + 5520) f_{c,cyl}^{0.41} \tag{4}$$

$$\sigma_c = \begin{cases} \varepsilon_c E_c & \varepsilon_c/\varepsilon_0 < 1/3 \\ f_{c,cyl} \frac{A(\varepsilon_c/\varepsilon_0)}{A - 1 + (\varepsilon_c/\varepsilon_0)^B} & \varepsilon_c/\varepsilon_0 \geq 1/3 \end{cases} \tag{5}$$

$$A = \begin{cases} B = \frac{\varepsilon_0 E_c}{\varepsilon_0 E_c - f_{c,cyl}} & \varepsilon_c/\varepsilon_0 \leq 1 \\ 1 + 0.723\, RI^{-0.957} & \varepsilon_c/\varepsilon_0 > 1 \end{cases} \tag{6}$$

$$B = \max\left\{ \left(\frac{f_{c,cyl}}{50} \right)^{0.064} \left(1 + 0.882 RI^{-0.882} \right), A \right\} \quad \varepsilon_c/\varepsilon_0 > 1 \tag{7}$$

where ε_0 is the strain at compressive strength, and E_c is the undamaged elastic modulus.

2.2.2. Uniaxial Tension Stress-Strain Relationship

The tensile strength of concrete is estimated as:

$$f_t = 0.56 f_{c,cyl}^{0.5} \tag{8}$$

The tensile stress-strain relationship of steel-fiber-reinforced concrete developed by [37] is adopted here:

$$\sigma_t = (1 - d) E_c (\varepsilon_t - \varepsilon_{pl}) \tag{9}$$

$$d = \begin{cases} 0 & \varepsilon_t \leq \varepsilon_{tu} \\ a + b e^{-c\varepsilon_t \times 10^6} & \varepsilon_t > \varepsilon_{tu} \end{cases} \tag{10}$$

$$a = 1 - 0.226RI \tag{11}$$

$$b = -1 + 0.238RI \tag{12}$$

$$c = 0.001 + 0.242 e^{-10RI} \tag{13}$$

$$\varepsilon_{pl} = \begin{cases} 0 & \varepsilon_t \leq \varepsilon_{tu} \\ 0.987\varepsilon_t - 78.291 \cdot 10^{-6} & \varepsilon_t > \varepsilon_{tu} \end{cases} \tag{14}$$

$$\varepsilon_{tu} = \frac{f_t}{E_c} \tag{15}$$

where ε_{pl} and ε_{tu} are the plastic strain and the strain corresponding to the tensile strength, respectively.

2.3. Reinforcing Bars Constitutive Law

The reinforcing bars are described by a typical elastic-plastic stress-strain law, whose parameters are listed in Table 3.

Table 3. Mechanical properties of reinforcing bars.

ID	Diameter (mm)	Area (mm^2)	Yield Strength f_y (MPa)	Yield Strain ε_y	Elastic Modulus (GPa)	Ultimate Tensile Strength f_u (Mpa)	Ultimate Tensile Strain ε_u
4	12.7	126.7	858	0.0039	220	1034	0.04
5	15.9	198.5	826	0.0038	217	1016	0.04
6	19.1	286.5	471	0.0024	196	696	0.04

2.4. Finite Element Type and Mesh

The SFRC is modeled with solid elements (C3D8R), along with a Concrete Damage Plasticity (CDP) Model. A variety of damage parameters proposed in [44–50] were examined and, after comparing their relative accuracy, those used in [46] were selected. The adopted damage variables, D_c and D_t, vary between 0 (undamaged) and 1 (fully damaged), as follows:

$$D_c = 1 - \frac{\sigma_c}{0.2\varepsilon_c^{in} E_c + \sigma_c} \tag{16}$$

$$D_t = 1 - \frac{\sigma_t}{f_t} \tag{17}$$

$$\varepsilon_c^{in} = \varepsilon_c - \frac{\sigma_c}{E_c} \tag{18}$$

$$\varepsilon_t^{ck} = \varepsilon_t - \frac{\sigma_t}{E_c} \tag{19}$$

where ε_c^{in} is the inelastic strain, ε_c^{ck} is the cracking strain, and E_c is the undamaged elastic modulus. Additional parameters of the CDP model are in Table 4.

Table 4. Plasticity parameters used in the CDP model.

Dilation angle, $\psi(^\circ)$	30
Eccentricity, ε	0.1
Stress ratio, f_{b0}/f_{c0}	1.16
Shape of the yielding surface, K_c	0.6667
Viscosity coefficient, μ	0.001

The optimal mesh was selected after a comparison among three different concrete grids (Table 5) in terms of crack pattern (Figure 2) and load-displacement curve (Figure 3). The selected mesh (concrete grid = 50), shown in Figure 4 and Table 6, is a reasonable compromise between accuracy and computational time. These conclusions also apply to the models of the other three walls, whose comparisons in terms of load–displacement curves are not shown in this section for the sake of space. However, they can be found in the next section, within the parametric analyses.

Table 5. Comparison of computational time among different concrete grids.

Concrete Grid (mm)	Computational Time (min)
40	104
50	85
70	67

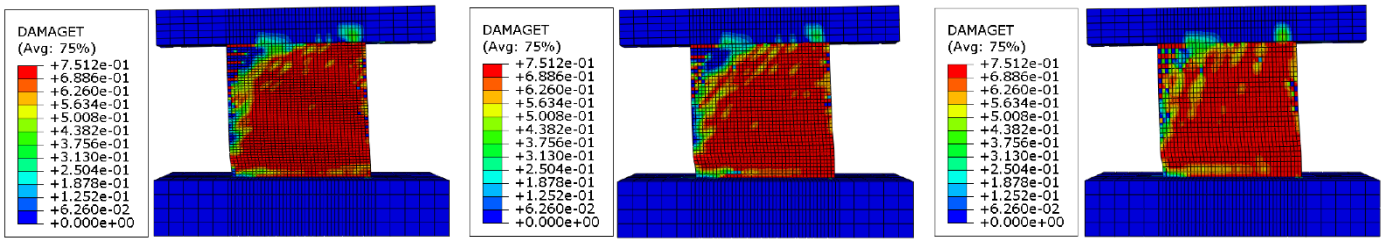

Figure 2. Comparison of crack patterns among different concrete grids. (**a**) Concrete grid = 40. (**b**) Concrete grid = 50. (**c**) Concrete grid = 70.

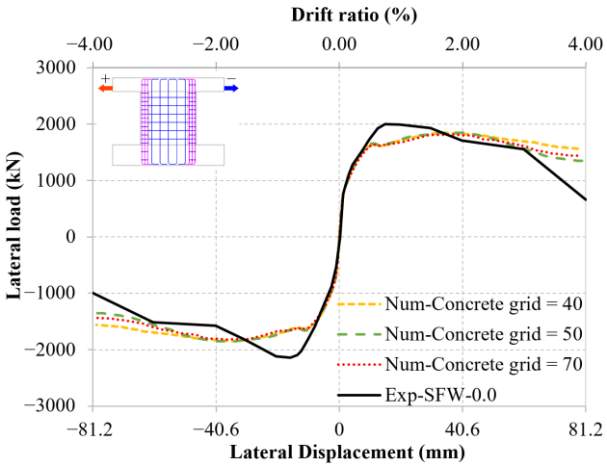

Figure 3. Accuracy of load–displacement curves with respect to experimental test SFW-0.0 using different concrete grids.

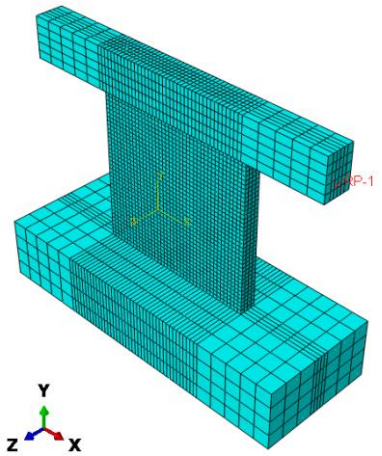

Figure 4. Mesh used in the model of the SFRC shear wall (concrete grid = 50).

Table 6. Parameters of finite element type and mesh.

ID	Concrete FE Type	Reinforcing Bars FE Type	Concrete Grid (mm)	Steel Bars Grid (mm)
Top Beam	C3D8R	T3D2	200	100
Wall	C3D8R	T3D2	50	50
Base beam	C3D8R	T3D2	200	100

2.5. Boundary Conditions and Load Application

The schematic illustration of the test setup geometry is shown in Figure 5, and the corresponding boundary condition and loading position and direction is shown in Figure 6. For the application of horizontal loading, in order to simulate the actual boundary conditions and avoid stress concentration, a point (the height of the point from the base top surface is 2030 mm) located on the side surface of the top beam is coupled with the four vertical planes of the top beam (Figure 7a). The steel reinforcement (T3D2 truss elements) is embedded within the concrete elements and fully bonded to them, as shown in Figure 7b. The analyses are carried out in three steps: (1) the bottom beam is fixed at the base (Figure 8), (2) a constant vertical load is applied (Figure 8a), (3) the horizontal load is applied (Figure 8b). The loading history of reference experimental study is shown in Table 7. It is worth noticing that, while in the reference tests each level was cycled three times, in the numerical analyses the load was applied monotonically to reduce the computational time. This implies that the accumulated damage in each cyclic sequence was neglected. However, because the comparisons carried out in the following section are based on monotonic quantities, the ensuing considerations can be maintained.

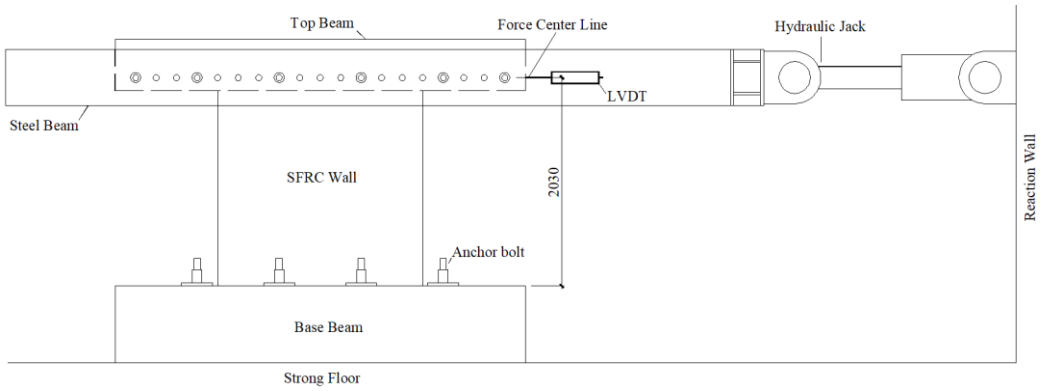

Figure 5. Schematic illustration of test setup details.

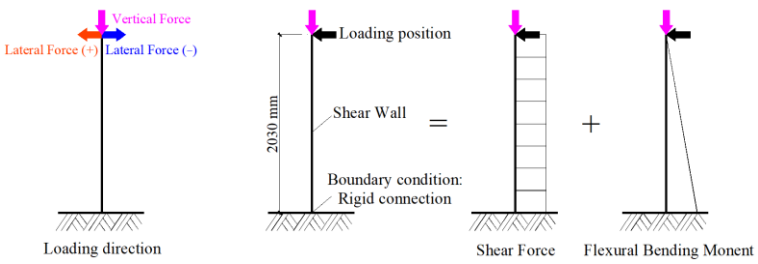

Figure 6. Shear wall boundary condition and loading position and direction.

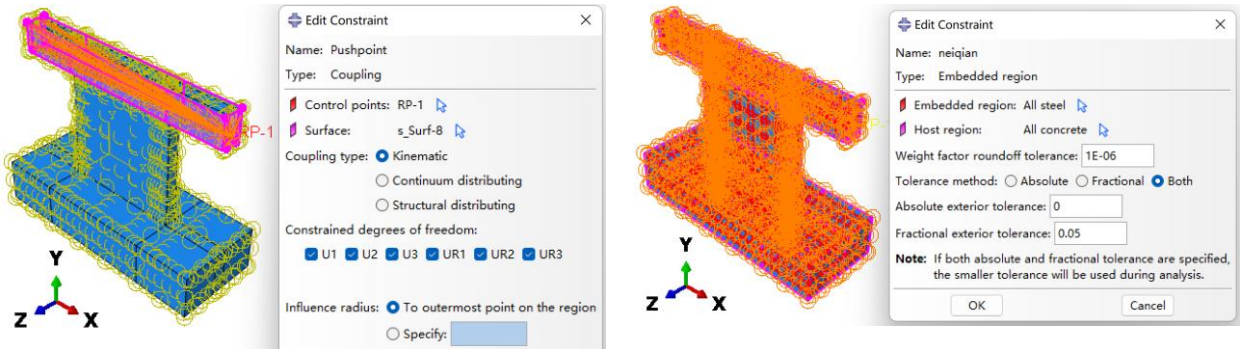

(**a**) (**b**)

Figure 7. Details of FE model (**a**) coupling of FE model; (**b**) embedded region of FE model.

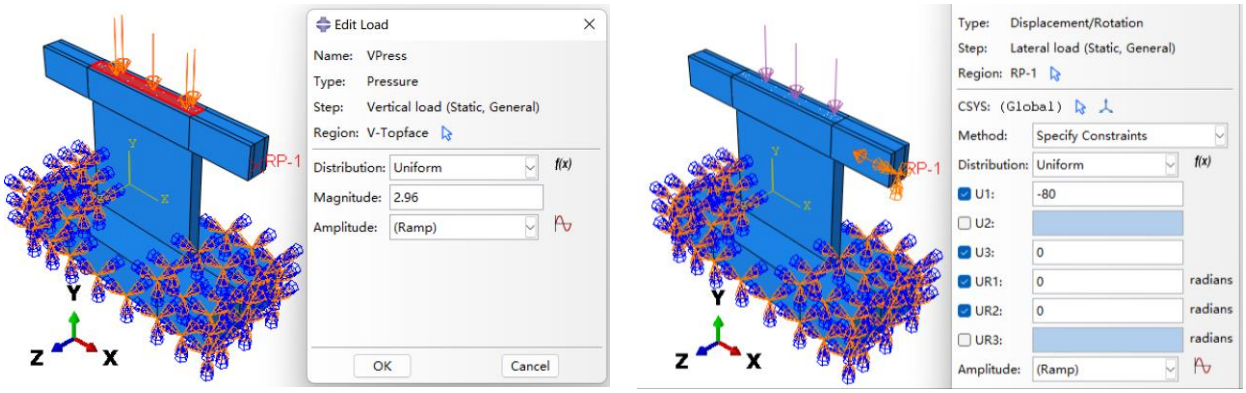

(**a**) (**b**)

Figure 8. Application of loads (**a**) vertical load of FE model; (**b**) horizontal load of FE model.

Table 7. Loading history of experimental tests [16] in terms of top displacements and drifts.

Disp (mm)	Drift (%) (=Disp/2030 mm)
2.54	0.125
5.08	0.25
7.61	0.375
10.15	0.5
15.23	0.75
20.30	1
30.45	1.5
40.60	2
60.90	3
81.20	4

3. Validation of the Finite Element Models and Numerical Analysis

In this section, numerical analyses are presented to explore the effects on the lateral response of SFRC shear walls of different ALRs, of different openings configurations, and of different reinforcement ratios. In these analyses, the FE models presented in the previous section were used, after being calibrated against the experimental tests by Huang [16]. Having obtained accurate predictions for all four tests considered, the FE models were then used to model the response of SFRC walls under different combinations, not considered in previous experimental tests, of ALR, openings, and reinforcement ratio (Table 8).

Table 8. Cases considered in the parametric study.

ID	ALR				Opening	Reinforcement Ratio
	0.00	0.15	0.35	0.55		
SFW	V, P	P	P	P	No	Normal
SFW60	V, P	P	P	P	No	Low
SFWO	V, P	P	P	P	Center window	Normal
SFWCD	V, P	P	P	P	Center door	Normal
SFWEO	P	P	P	P	Eccentric window	Normal
SFWED	P	P	P	P	Eccentric door	Normal
SFWEO60	P	-	-	-	Eccentric window	Low
SFWED60	P	-	-	-	Eccentric door	Low

V = experimental validation, P = parametric study.

3.1. Specimens for the Parametric Study

The specimens considered in the parametric study are shown in Figure 9 and ALRs of SFRC shear walls are list in Table 9.

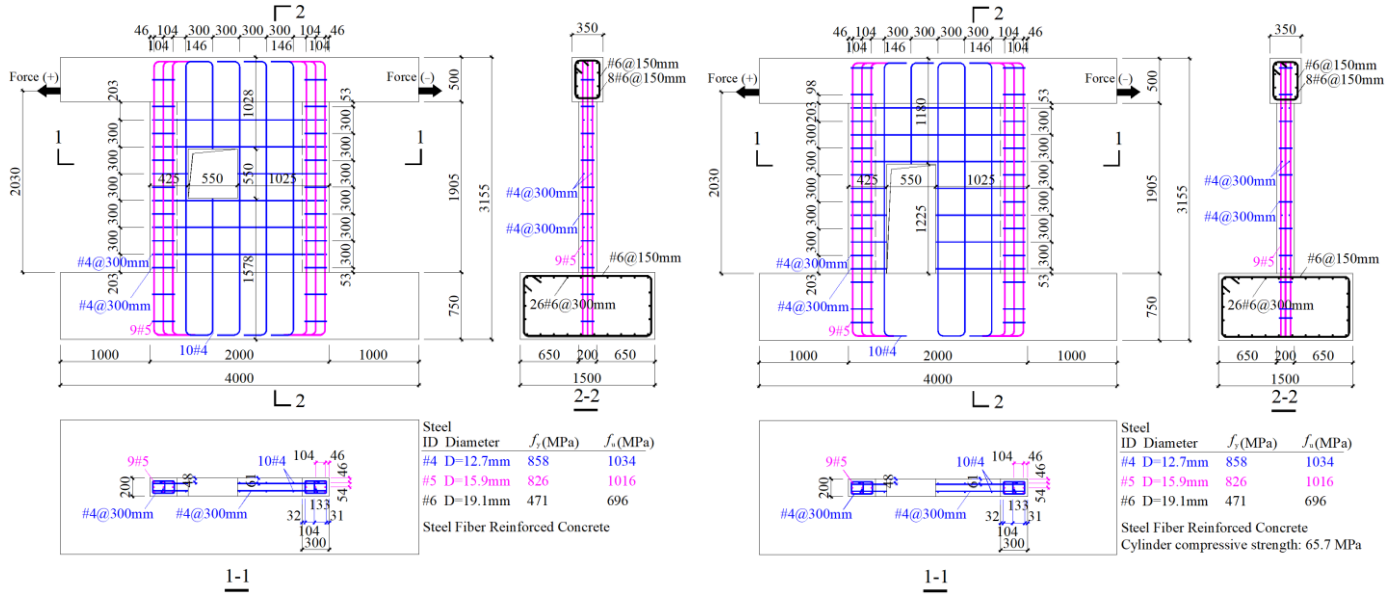

(**a**) (**b**)

Figure 9. *Cont.*

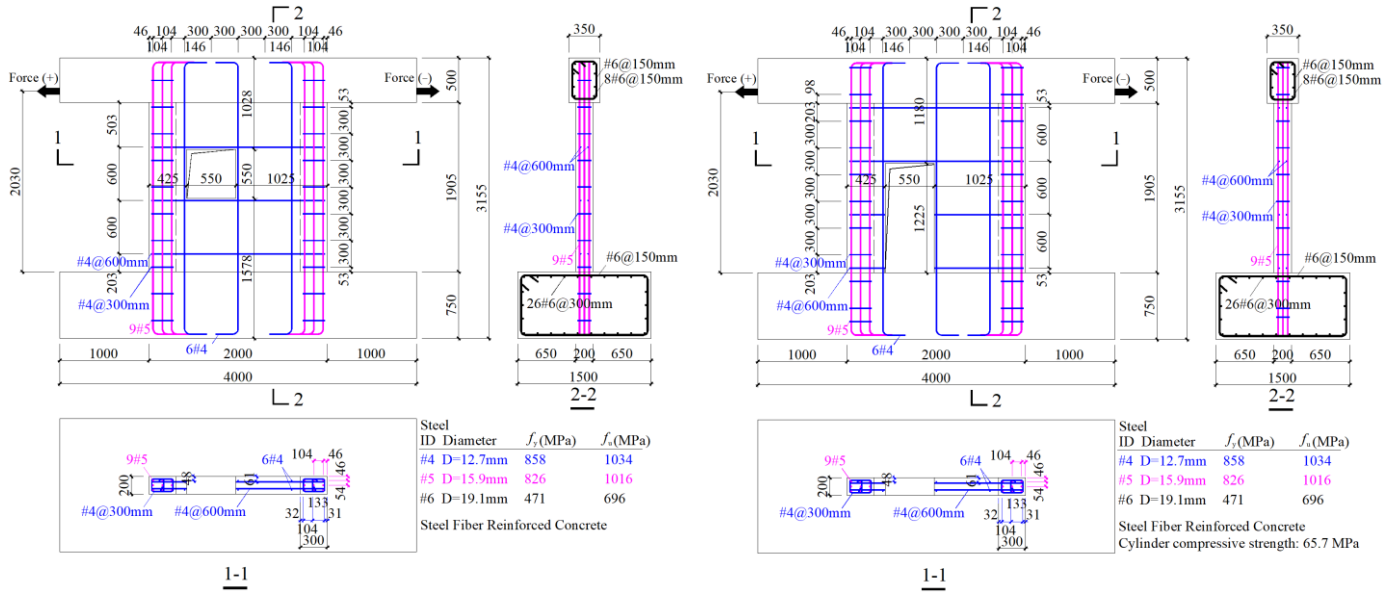

(**c**) (**d**)

Figure 9. Geometry and reinforcement of the specimens for the parametric study: (**a**) SFWEO, (**b**) SFWED, (**c**) SFWEO60, (**d**) SFWED60, in addition to those shown in Figure 1.

Table 9. ALRs of SFRC shear walls.

ALR	$f_{c,cyl}$ (MPa)	A_{cb} (mm^2)	N (kN)
0.0	65.7	120,000	0
0.15	65.7	120,000	1183
0.35	65.7	120,000	2759
0.55	65.7	120,000	4336

Axial Load Ratio (ALR)

The ALR is one of the main parameters considered in the parametric analyses. Two definitions (Figure 10) can be adopted for ALR: (1) considering the whole cross-section, Equations (20) and (2) considering only the boundary elements, Equation (21). In this study, the latter is adopted and four values, 0.0, 0.15, 0.35, and 0.55, are considered.

$$\mathrm{ALR} = \frac{N}{f_{c,cyl} A_c} \tag{20}$$

$$\mathrm{ALR} = \frac{N}{f_{c,cyl} A_{cb}} \tag{21}$$

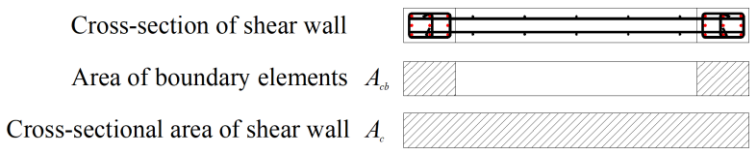

Figure 10. Different estimates of the shear area of a shear wall with boundary elements.

3.2. Classification of Failure Modes

Starting from the classification of failure modes in RC shear walls by Paulay et al. [51] and by Zhang et al. [52], some further elaborations are presented hereafter. Failure modes

occurring in RC walls depend on size, reinforcement arrangement, and material properties [51]. Lateral loading in SFRC shear walls generates bending moment and shear, which cause flexural failure and shear failure. Thus, the actual failure mode results from a combination of these two modes. A matrix is hereafter proposed to classify the shear wall failure modes, as shown in Table 10, where it can be noticed that:

(1) Flexural failure modes can be divided into four damage levels:
   a. Undamaged (F0);
   b. With sub-horizontal flexural cracks (F1);
   c. With sub-horizontal flexural cracks and corner concrete crushing (F2);
   d. With sub-horizontal flexural cracks and base concrete crushing (F3).

(2) Shear failure modes can be divided into four damage levels:
   a. Undamaged (S0);
   b. With diffused diagonal shear cracks (S1);
   c. With wide diagonal shear cracks (S2);
   d. With significant diagonal compression crushing (S3).

Table 10. Matrix of shear wall failure modes and corresponding damage levels (N.B. To the author's knowledge, F3 and S2 and F3 and S3 failure modes rarely occur).

Shear-Induced Damage Levels	Flexure-Induced Damage Levels: F0	F1	F2	F3
S0	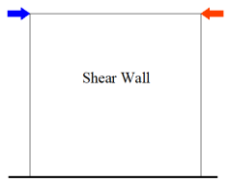	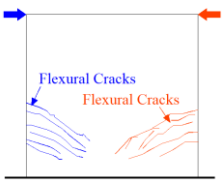	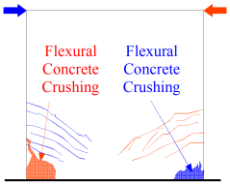	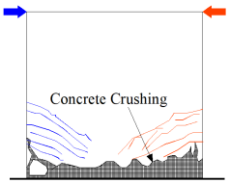
S1	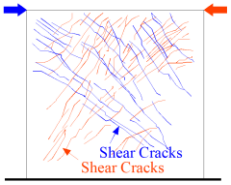	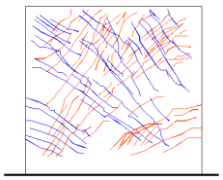	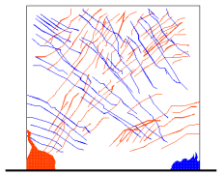	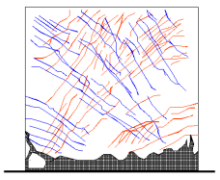
S2	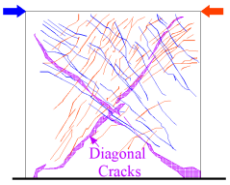	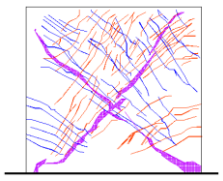	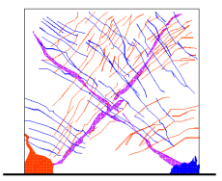	None
S3	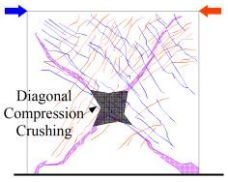	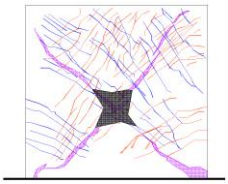	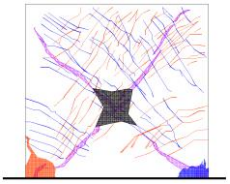	None

3.2.1. Specimen SFW (No Opening, Normal Reinforcement Ratio)

Figure 11 shows the failure mode of the reference specimen SFW, which is a combination of F3 and S1. The test terminates at drift ratio of 4%, with a displacement of 81.2 mm.

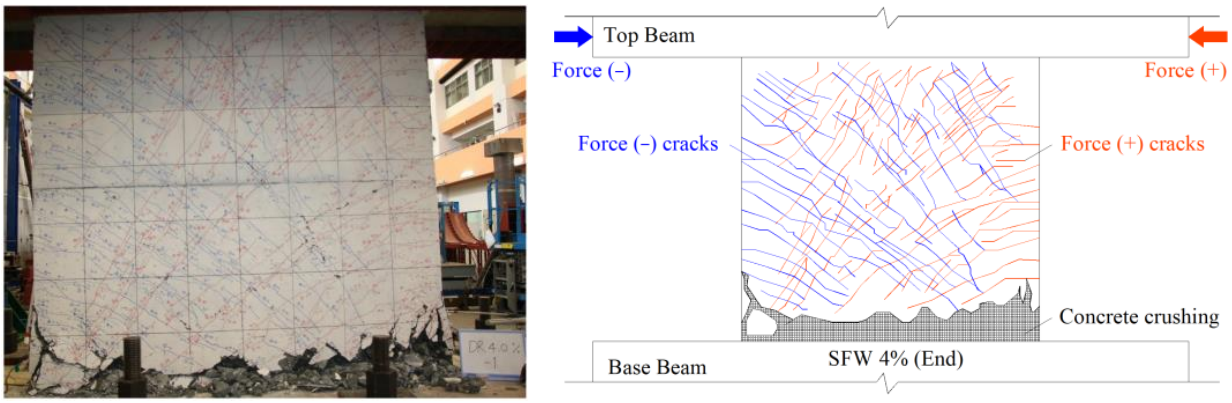

Figure 11. Specimen SFW: failure mode. (**a**) Failure mode photo [16]. (**b**) Failure mode schematic.

Figure 12 shows the comparison of the skeleton curves between test and numerical results. With ALR = 0.0, a good agreement is achieved. As ALR increases, the lateral load capacity and stiffness increase and show a positive correlation with ALR while its post-peak stage, higher ALRs result in decrease in lateral load capacity. In the end of post-peak stage, the relationship between lateral load capacity and ALRs is reversed, showing a negative correlation.

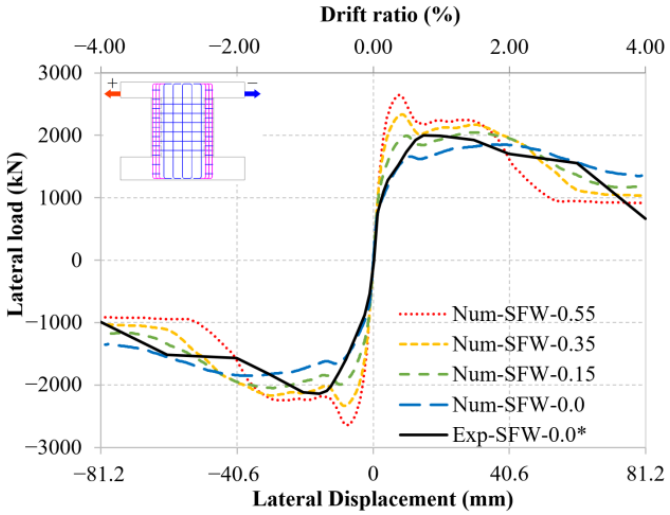

Figure 12. Specimen SFW: comparison of skeleton curves between test and numerical results. (*) denotes that the data were obtained from the experimental tests by Huang [16].

Table 11 presents the comparison of the strain distributions and crack patterns of specimen SFW between the numerical results with ALR = 0.0 and with ALR = 0.55. It is found that the flexural damage level decreases (the flexural cracks widths and the flexure-induced strains decrease), while the shear damage level increases (the shear cracks widths and the flexure-induced strains increase), indicating that higher ALR values shift the prevailing failure mechanism from flexural to shear.

Table 11. Specimen SFW: strain distributions and crack patterns as represented by the damage indices.

	Strain Distribution	Damage Index D_t	Damage Index D_c
ALR = 0.0	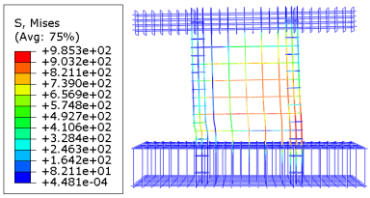	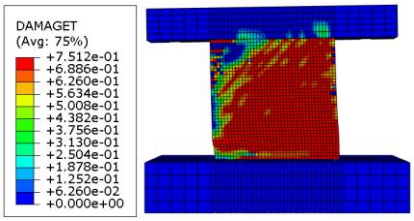	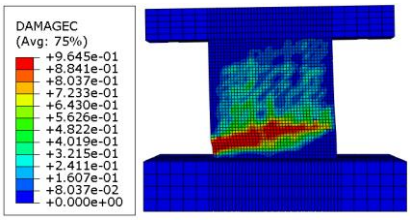
ALR = 0.55	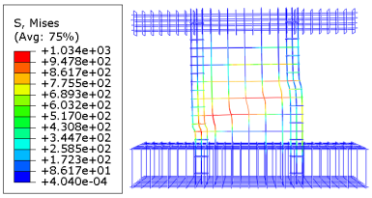	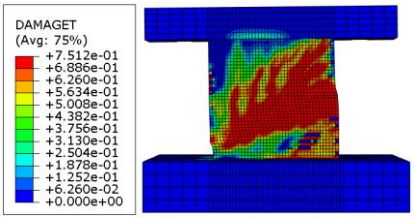	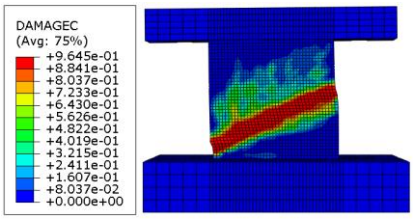

3.2.2. Specimen SFW60 (No Opening, Low Reinforcement Ratio)

Figure 13 shows the failure mode of the reference specimen SFW60, which is a combination of F1 and S2 (also known as diagonal compression failure). The test ends at drift ratio of 2%, with a displacement of 40.6 mm. Compared to specimen SFW, it is found that low reinforcement ratio results in two significant diagonal cracks across the wall, which indicate an increase in shear damage level.

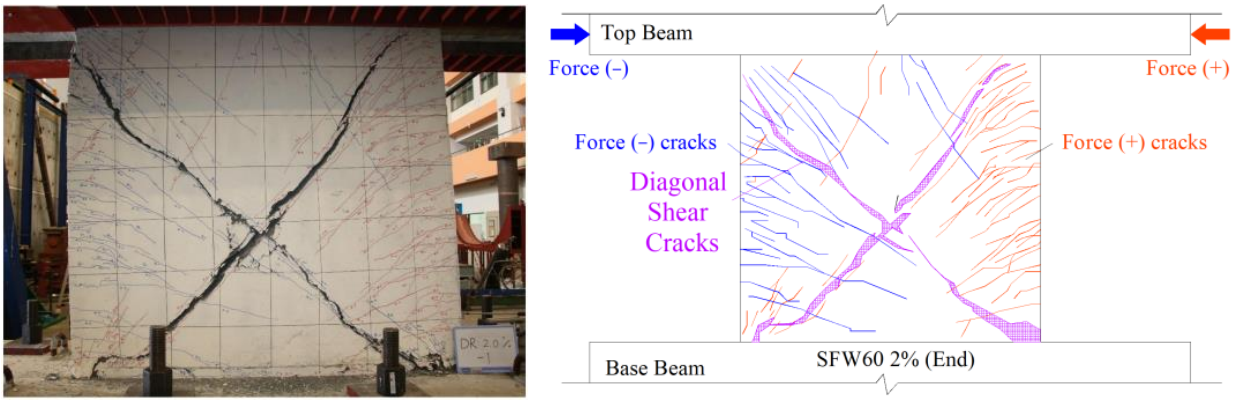

(**a**) (**b**)

Figure 13. Specimen SFW60: failure mode. (**a**) Failure mode photo [16]. (**b**) Failure mode schematic.

Figure 14 shows the comparison of the skeleton curves between test and numerical results. As ALR increases, significant increase in load capacity and stiffness is observed; however, the skeleton curve of SFW60 shows a steeper post-peak degradation than SFW. This is because higher ALRs switch the prevailing failure mechanism from flexural to shear and low reinforcement ratio reduces the resistance to shear damage.

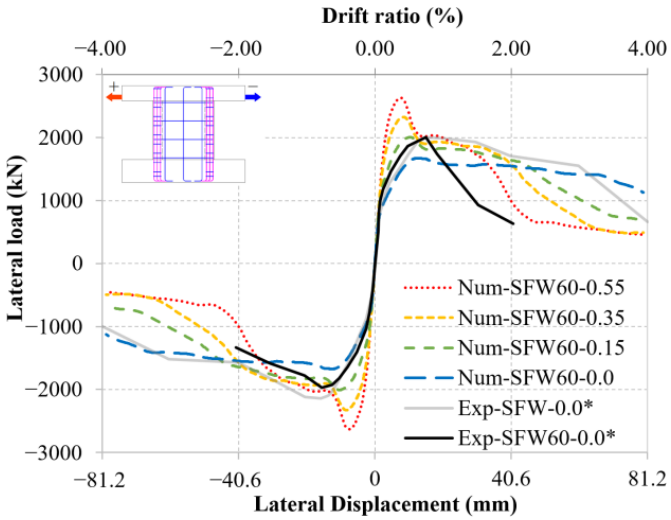

Figure 14. Specimen SFW60: comparison of skeleton curves between test and numerical results. (*) denotes that the data were obtained from the experimental tests by Huang [16].

Table 12 presents the comparison of the strain distributions and crack patterns of specimen SFW60 between the numerical results with ALR = 0.0 and ALR = 0.55. It is found that the flexural damage level decreases (the flexural cracks widths and the flexure-induced strains decrease), while the shear damage level increases (the shear cracks widths and the flexure-induced strains increase).

Table 12. Specimen SFW60: strain distributions and crack patterns as represented by the damage indices.

	Strain Distribution	Damage Index D_t	Damage Index D_c
ALR = 0.0	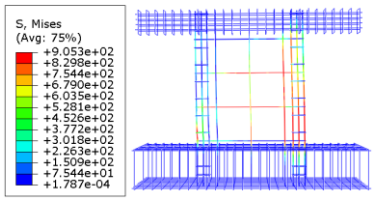	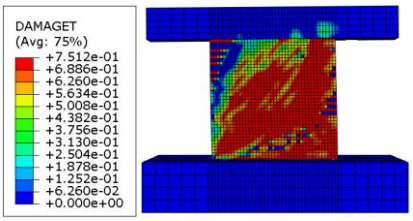	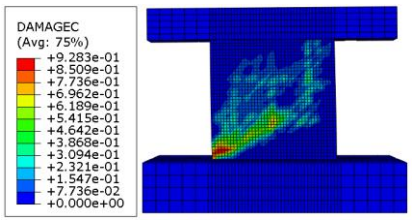
ALR = 0.55	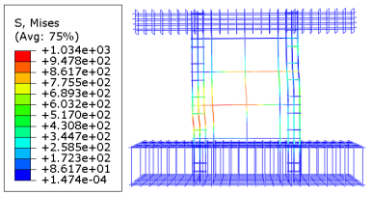	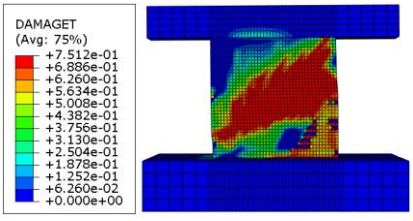	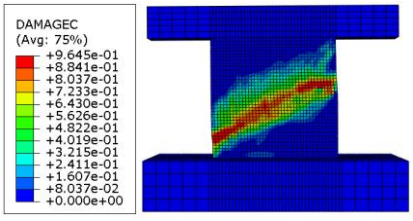

3.2.3. Specimen SFWO (Center Window Opening, Normal Reinforcement Ratio)

Figure 15 shows the failure mode of the reference specimen SFWO, which is a combination of F1 and S2. The test ends at drift ratio of 2%, with a displacement of 40.6 mm.

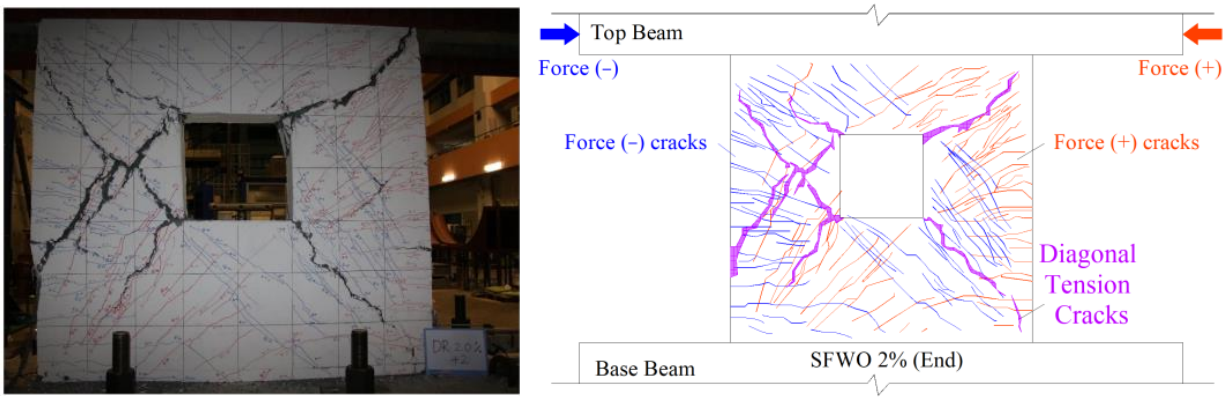

(**a**) (**b**)

Figure 15. Specimen SFWO: failure mode. (**a**) Failure mode photo [16]. (**b**) Failure mode schematic.

Figure 16 shows the comparison of the skeleton curves between test and numerical results. Compared to SFW, specimen with door opening does not show significant decrease in lateral load capacity. As ALR increases, the lateral load capacity and stiffness of the shear wall increase while the deformation capacity decreases.

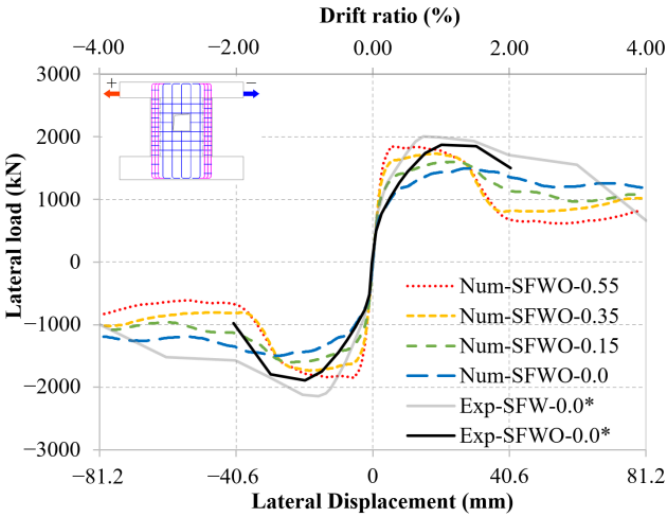

Figure 16. Specimen SFWO: comparison of skeleton curves between test and numerical results. (*) denotes that the data were obtained from the experimental tests by Huang [16].

Table 13 presents the comparison of the strain distributions and crack patterns of specimen SFWO between the numerical results with ALR = 0.0 and ALR = 0.55. In this latter case, the high strain and damage index concentrates within the diagonal area around the opening of the shear wall. Moreover, the highest strain occurs at the upper corner and bottom corner of the center window opening. The results show that the shear damage domains the failure pattern for the shear wall with ALR = 0.55.

Table 13. Specimen SFWO: strain distributions and crack patterns as represented by the damage indices.

	Strain Distribution	Damage Index D_t	Damage Index D_c
ALR = 0.0	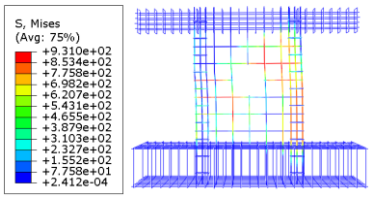	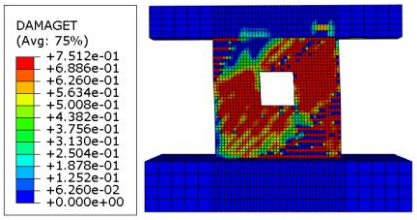	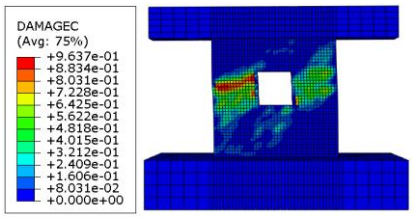
ALR = 0.55	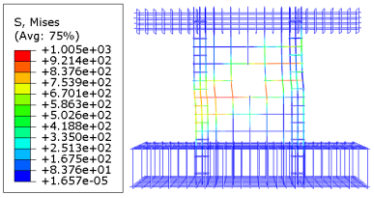	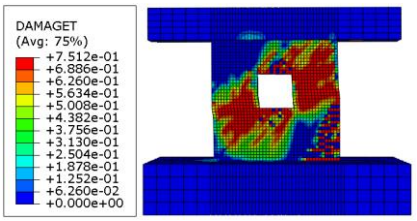	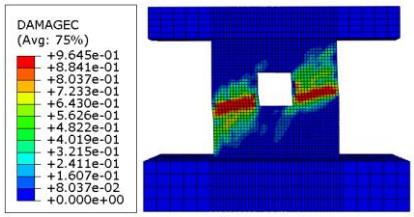

3.2.4. Specimen SFWCD (Center Door Opening, Normal Reinforcement Ratio)

Figure 17 shows the failure mode of the reference specimen SFWCD, which is a combination of F2 and S2. The test ends at drift ratio of 3%, with a displacement of 60.9 mm.

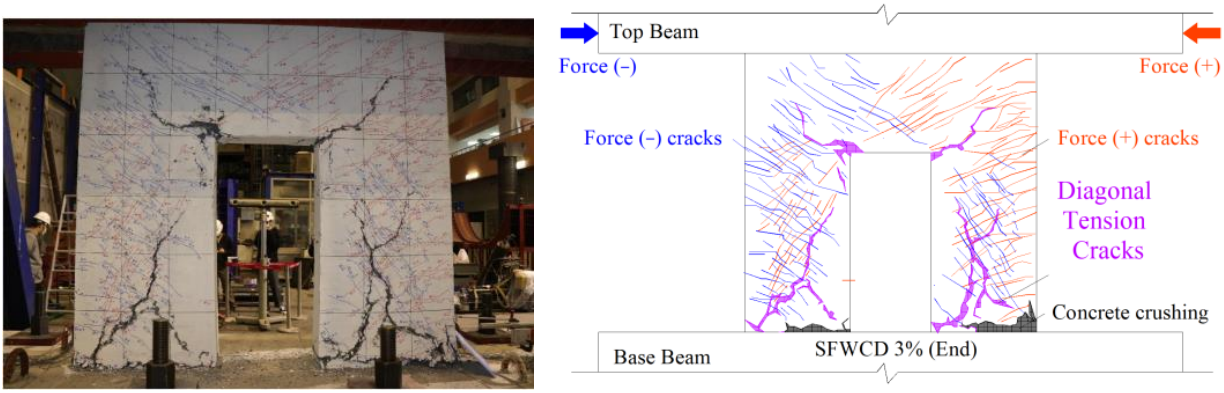

(**a**) (**b**)

Figure 17. Specimen SFWCD: failure mode. (**a**) Failure mode photo [16]. (**b**) Failure mode schematic.

Figure 18 shows the comparison of the skeleton curves between test and numerical results. As ALR increases, the shear wall lateral load capacity and stiffness increase, but the deformation capacity does not decrease significantly. This is because two slender wall-branches on both sides of the door opening form flexural bearing system, thus contributing to the overall deformation capacity. Compared to SFWO, the ductility of this specimen with door opening does not show significant decrease with ALR increases. Therefore, window openings can be replaced by door openings with flexible materials fill the bottom space of door openings, which not only satisfies the needs of architectural functions of windows but also benefits the lateral ductility and deformation capacity of the shear wall.

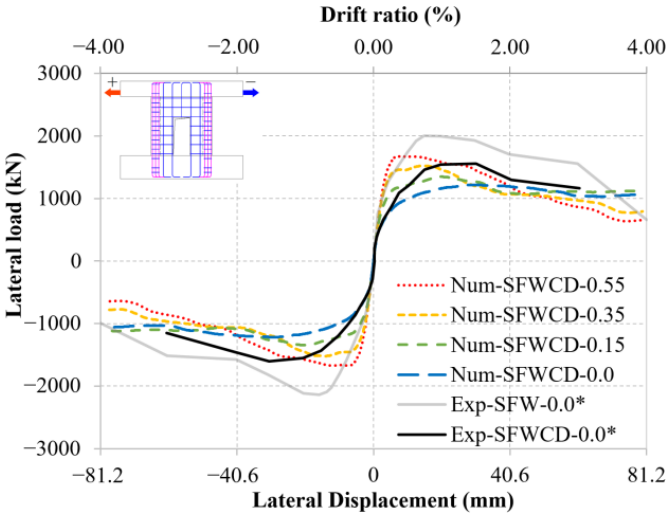

Figure 18. Specimen SFWCD [16]: comparison of skeleton curves between test and numerical results. (*) denotes that the data were obtained from the experimental tests by Huang [16].

Table 14 presents the comparison of the strain distributions and crack patterns of specimen SFWCD between the numerical results with ALR = 0.0 and ALR = 0.55. It is found that the flexural damage level decreases (the flexural cracks widths and the strain caused by flexural failure decrease), while the shear damage level increases (the shear cracks widths and the strain caused by flexural failure increase).

Table 14. Specimen SFWCD: strain distributions and crack patterns as represented by the damage indices.

	Strain Distribution	**Damage Index D_t**	**Damage Index D_c**
ALR = 0.0	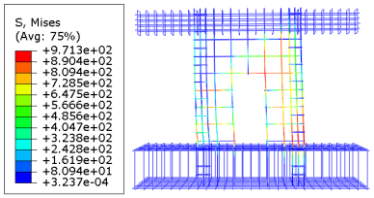	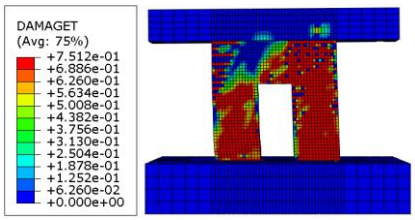	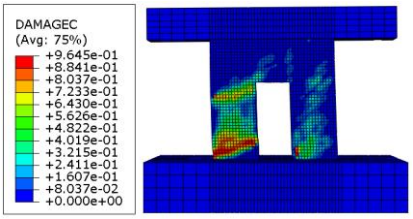
ALR = 0.55	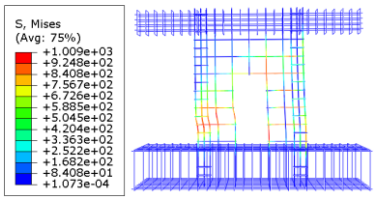	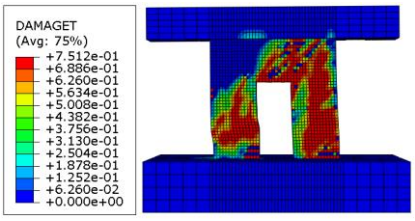	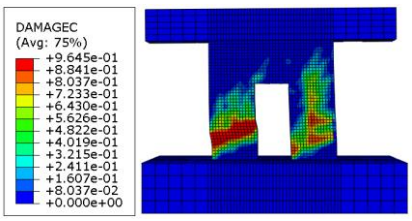

3.2.5. Specimen SFWEO (Eccentric Window Opening, Normal Reinforcement Ratio) and SFWEO60 (Eccentric Window Opening, Low Reinforcement Ratio)

Table 15 shows the failure mode of the numerical specimen SFWEO, which is a combination of F1 and S2. The numerical test ends at a drift ratio of 2%, with a displacement of 40.6 mm. Table 15 presents the comparison of the strain distributions and crack patterns of specimen SFWEO between the numerical results with ALR = 0.0 and ALR = 0.55. In this latter case, it is found that the flexural damage level is decreased (the flexural cracks widths and the strain caused by flexural failure decrease), while the shear damage level increases (the shear cracks widths and the strain caused by flexural failure increase).

Table 15. Specimen SFWEO: strain distributions and crack patterns as represented by the damage indices.

	Strain Distribution	Damage Index D_t	Damage Index D_c
ALR = 0.0 Force (+)	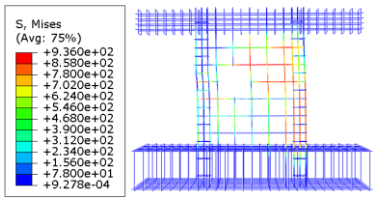	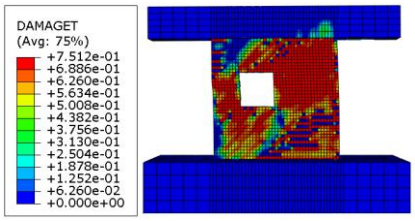	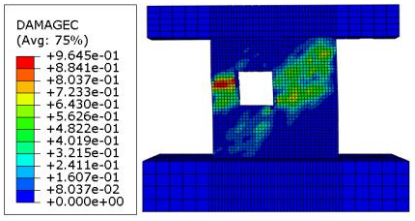
ALR = 0.55 Force (+)	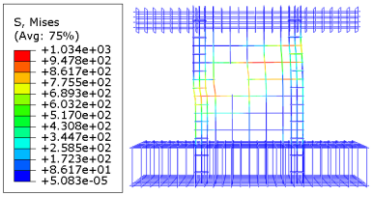	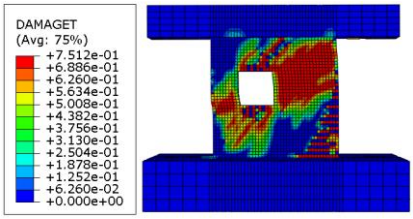	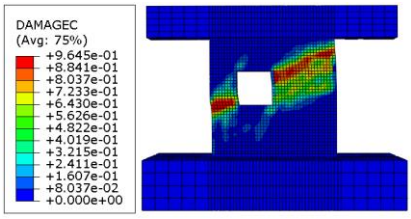
ALR = 0.0 Force (−)	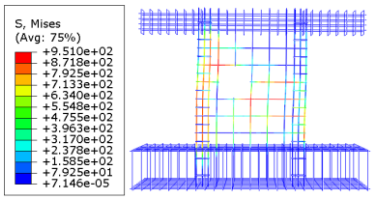	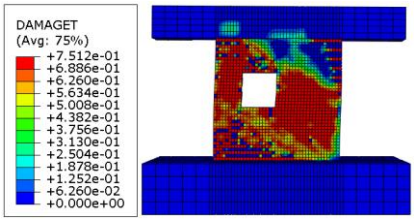	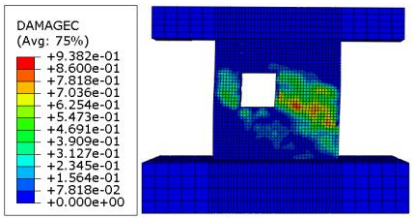
ALR = 0.55 Force (−)	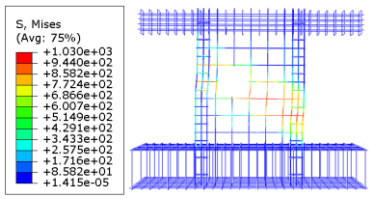	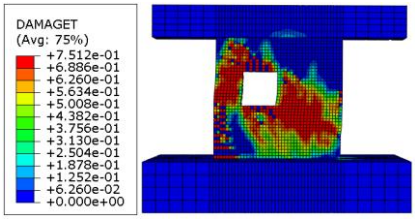	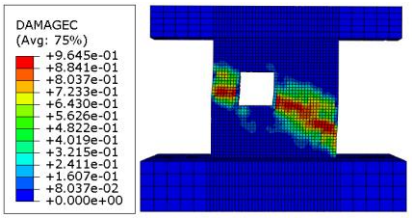

Figure 19 shows the comparison of the skeleton curves between numerical results of SFWEO and experimental results of SFW and SFWO. It is found that in case of eccentric window opening, the load capacity does not significantly depend on the loading direction, which could be explained by the improvement of concrete tensile strength by steel fiber. To further discover the reasons, this paper study the effect of reinforcement ratio. Figure 20 shows the comparison of the skeleton curves between numerical results of SFWEO and SFWEO60. It is found that as reinforcement ratio decreases, the differences in the lateral load capacity under push and pull loading directions increases.

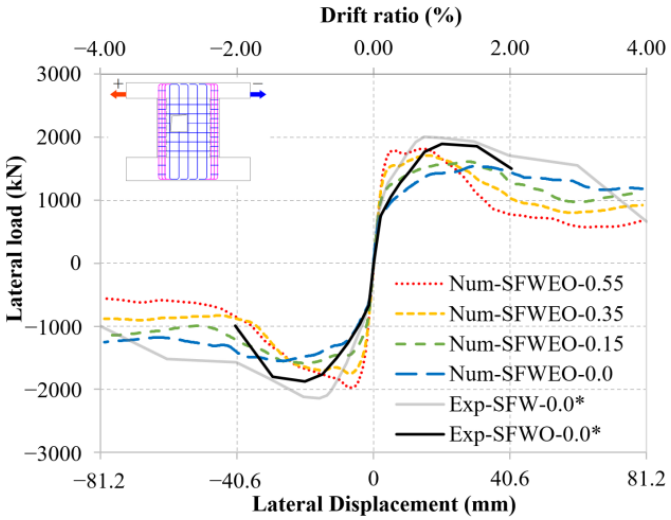

Figure 19. Specimen SFWEO: comparison of skeleton curves between numerical results of SFWO and SFWEO. (*) denotes that the data were obtained from the experimental tests by Huang [16].

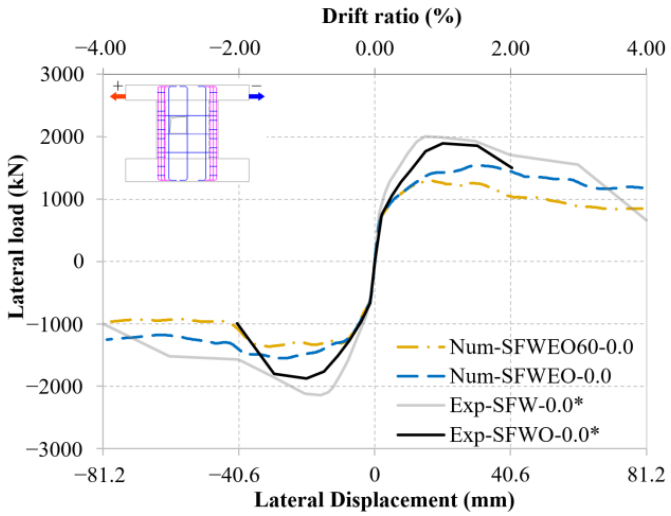

Figure 20. Specimen SFWEO60: comparison of skeleton curves between numerical results of SFWEO and SFWEO60. (*) denotes that the data were obtained from the experimental tests by Huang [16].

3.2.6. Specimen SFWED (Eccentric Door Opening, Normal Reinforcement Ratio) and SFWED60 (Eccentric Door Opening, Low Reinforcement Ratio)

Table 16 shows the failure mode of the numerical specimen SFWED, which is a combination of F2 and S2. The numerical test ends at a drift ratio of 3%, with a displacement of 60.9 mm. Table 16 presents the comparison of the strain distributions and crack patterns of specimen SFWED between the numerical results with ALR = 0.0 and ALR = 0.55. It is found that the flexural damage level decreases (the flexural cracks widths and the strain caused by flexural failure decrease), while the shear damage level increases (the shear cracks widths and the strain caused by flexural failure increase). The largest compressive damage moves from the shear wall bottom to mid-height.

Table 16. Specimen SFWED: strain distributions and crack patterns as represented by the damage indices.

	Strain Distribution	Damage Index D_t	Damage Index D_c
ALR = 0.0 Force (+)	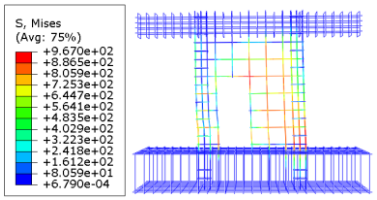	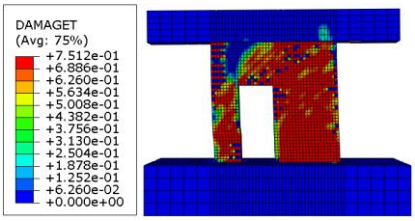	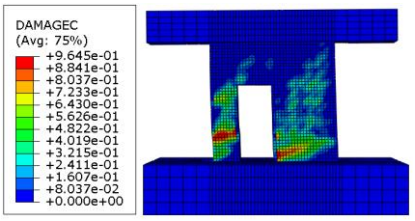
ALR = 0.55 Force (+)	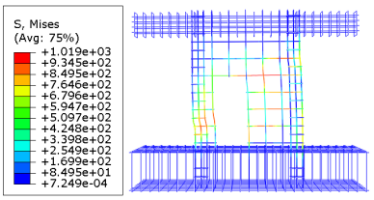	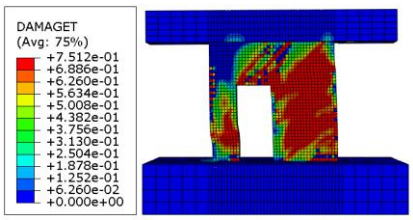	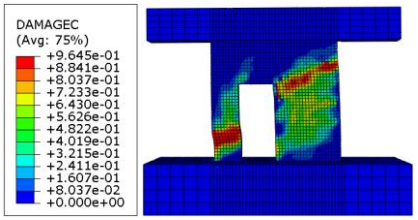
ALR = 0.0 Force (−)	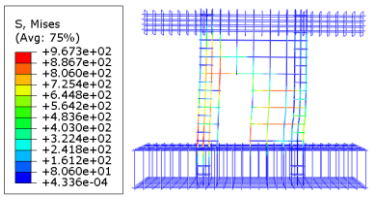	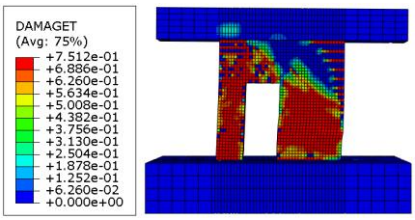	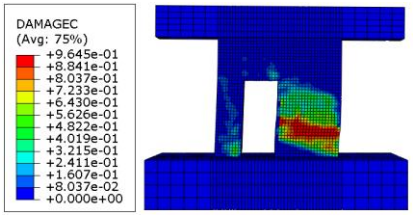
ALR = 0.55 Force (−)	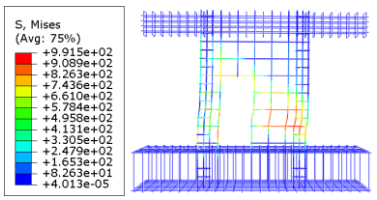	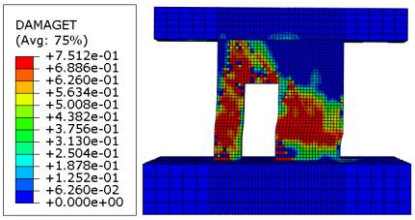	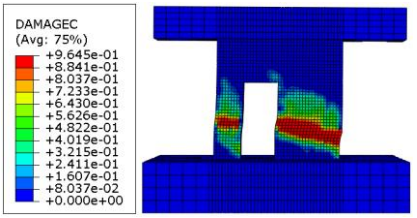

Figure 21 shows the comparison of the skeleton curves between numerical results of SFWED and experimental results of SFW and SFWCD. As ALR increases, the lateral load capacity and stiffness of the shear wall increase, while the deformation capacity does not decrease significantly. This is because two slender walls-branches form on both sides of the door opening, thus contributing to the overall deformation capacity. Figure 22 shows the comparison of the skeleton curves between numerical results of SFWED and SFWED60. It is found that as reinforcement ratio decreases, the differences in the lateral load capacity under push and pull loading directions increases, compared to window openings, these differences of door openings are more significant.

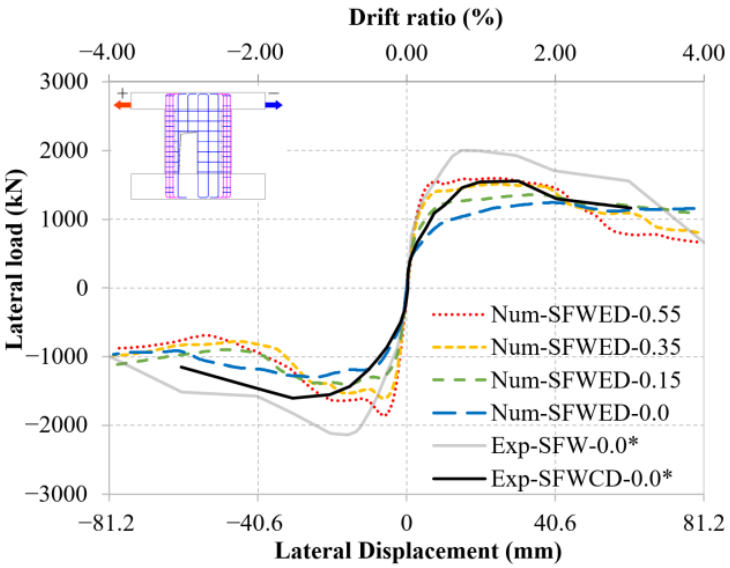

Figure 21. Specimen SFWED: comparison of skeleton curves between numerical results of SFWCD and SFWED. (*) denotes that the data were obtained from the experimental tests by Huang [16].

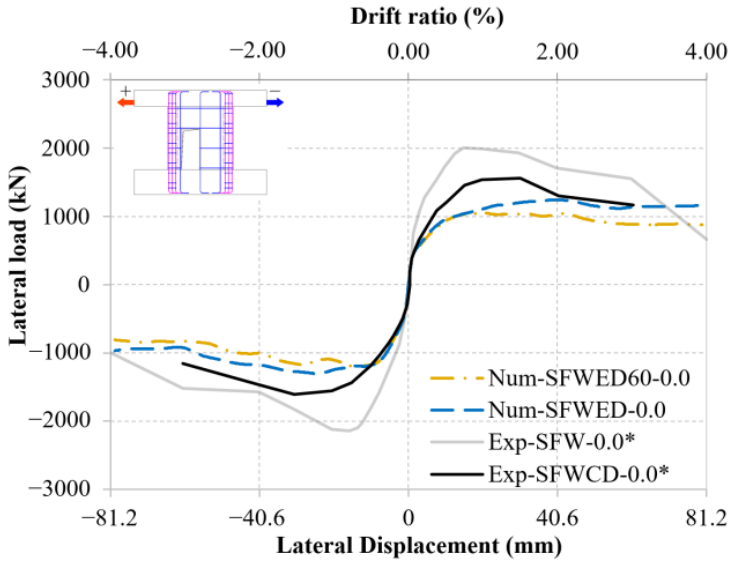

Figure 22. Specimen SFWED60: comparison of skeleton curves between numerical results of SFWED and SFWED60. (*) denotes that the data were obtained from the experimental tests by Huang [16].

3.3. Estimate of Ductility

Ductility expresses the deformation capacity of structures in the plastic range. The ductility index μ_d is defined as:

$$\mu_d = D_u / D_y \tag{22}$$

where D_u is the ultimate displacement, here defined at 0.85 of post-yield peak load, D_y is the displacement at yield load, defined as the point where tension reinforcement yields, while the post-yield peak load is defined as the maximum load in the post-yield branch (Figure 23).

Table 17 presents the comparison of the ductility indices calculated from the numerical results.

Figure 24 presents the comparison of the ductility capacity of specimens among the numerical results with ALR = 0.0, 0.15, 0.35, and 0.55. It is found that as ALR increases, the ductility capacity of the walls decreases. The decrease in the entire transverse reinforcement

in specimen SFW60, both in the end portions and in the center wall, gives a decrease in ductility compared with SFW. In cases of eccentric openings, the ductility capacity is affected by the loading direction. The ductility capacity in the presence of center opening lies between the two ductility capacities (+ and −) of the cases with eccentric openings.

Table 17. Ductility index of SFRC shear walls specimens.

ID	Force Direction	ALR	Yield Point		Post-Yield Peak Point		Ultimate Point		Ductility Index
			Drift Ratio at Yield (%)	Yield Force (MN)	Drift Ratio at Post-Yield Peak (%)	Post-Yield Peak Force (MN)	Drift Ratio at Ultimate (%)	85% of Post-Yield Peak Force (MN)	μ_d (=D_u/D_y)
SFW	(+), (−)	0	0.50	1.70	1.90	1.80	3.10	1.53	6.2
		0.15	0.48	2.00	1.55	2.05	2.40	1.74	5.0
		0.35	0.42	2.30	1.00	2.20	2.05	1.87	4.9
		0.55	0.39	2.70	0.90	2.30	1.70	1.96	4.4
SFW60	(+), (−)	0	0.53	1.70	1.70	1.60	3.70	1.36	7.0
		0.15	0.48	2.00	1.40	1.70	2.40	1.45	5.0
		0.35	0.43	2.30	1.00	1.90	2.00	1.62	4.7
		0.55	0.40	2.70	0.80	2.00	1.60	1.70	4.0
SFWO	(+), (−)	0	0.40	1.20	1.40	1.50	4.00	1.28	10.0
		0.15	0.35	1.40	1.10	1.60	1.90	1.36	5.4
		0.35	0.30	1.60	0.80	1.70	1.45	1.45	4.8
		0.55	0.30	1.80	0.60	1.80	1.40	1.53	4.7
SFWEO	(+)	0	0.30	1.00	0.80	1.35	3.40	1.15	11.3
		0.15	0.23	1.25	0.75	1.50	2.50	1.28	10.9
		0.35	0.25	1.55	0.73	1.70	1.50	1.45	6.0
		0.55	0.30	1.80	0.70	1.80	1.50	1.53	5.0
	(−)	0	−0.40	−1.20	−0.90	−1.40	−3.20	−1.19	8.0
		0.15	−0.35	−1.40	−0.80	−1.60	−1.90	−1.36	5.4
		0.35	−0.33	−1.70	−0.75	−1.70	−1.45	−1.45	4.4
		0.55	−0.35	−1.95	−0.70	−1.80	−1.15	−1.53	3.3
SFWCD	(+), (−)	0	0.35	0.90	1.30	1.20	3.00	1.02	8.6
		0.15	0.30	1.20	0.90	1.35	2.20	1.15	7.3
		0.35	0.30	1.45	0.80	1.55	1.60	1.32	5.3
		0.55	0.35	1.70	0.60	1.70	1.55	1.45	4.4
SFWED	(+)	0	0.45	0.90	2.00	1.30	4.00	1.11	8.9
		0.15	0.40	1.20	1.70	1.40	3.80	1.19	9.5
		0.35	0.38	1.40	1.00	1.50	2.60	1.28	6.8
		0.55	0.35	1.60	0.70	1.60	2.30	1.36	6.6
	(−)	0	−0.60	−1.20	−1.20	−1.25	−2.80	−1.06	4.7
		0.15	−0.40	−1.44	−0.80	−1.44	−1.80	−1.22	4.5
		0.35	−0.35	−1.60	−0.80	−1.60	−1.55	−1.36	4.4
		0.55	−0.35	−1.80	−0.95	−1.70	−1.35	−1.45	3.9

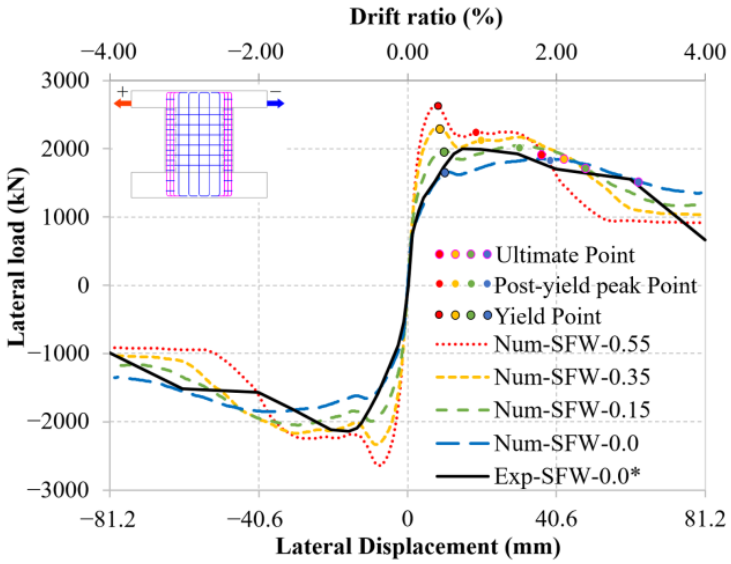

Figure 23. Example of determination of displacements at yield, post-yield peak load, and ultimate. (*) denotes that the data were obtained from the experimental tests by Huang [16].

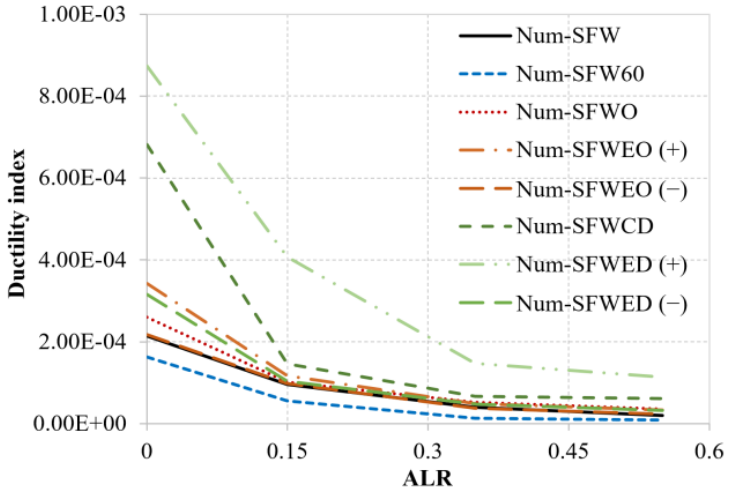

Figure 24. Comparison of ductility capacity of specimens.

4. Conclusions

A numerical investigation of the lateral capacity of shear walls made of steel-fiber-reinforced concrete (SFRC) was carried out, with the purpose of studying the effects, both of door and window openings, and of the axial load ratio (ALR). For the numerical investigation, finite element models were implemented based on the SFRC walls tested by Huang [16], which served as benchmark to calibrate their accuracy. After assessing the numerical model accuracy, a set of parametric analyses was carried out to study the effects of the ALR, of different opening configurations, and of the reinforcement ratio. Load–displacement curves, failure modes, crack patterns, and strain distributions were used as terms of comparison. The main conclusions of this study can be summarized as follows:

1. A classification of the shear wall failure modes is proposed, where it is observed that, as ALR increases, the flexural-induced damage decreases, while the shear-induced damage increases, thus reducing both ductility and deformation capacity, as shown in the last section.

2. As ALR increases, both lateral load capacity and stiffness increase and show a positive correlation with ALR while in the final post-peak stage, the relationship between lateral load capacity and ALRs is reversed, showing a negative correlation.
3. Even in the presence of window or door openings, and with ALR up to 0.55, the specimens still show relatively good lateral load and deformation capacity, thanks to the improvement introduced by the SFRC.
4. In general, window openings tend to reduce the lateral deformation capacity, while door openings tend to reduce the lateral load capacity. Therefore, if the lateral deformation capacity is of concern, window openings can be preferably obtained from door openings with a flexible infill at the bottom.
5. In the case of eccentric openings, as the reinforcement ratio decreases, the difference in the lateral load capacity in opposite directions increases. This phenomenon is more significant with door than with window openings.

Having ascertained the role of the parameters considered in this paper, further studies are currently under way to explore the role of other parameters, for example, the ratio between the openings size and the shear wall size.

Author Contributions: Conceptualization, Z.L., H.Z. and G.M.; methodology, Z.L., H.Z. and G.M.; software, Z.L., H.Z., G.M. and C.C.; validation, Z.L., H.Z. and G.M.; formal analysis, Z.L., H.Z. and G.M.; investigation, Z.L., H.Z. and G.M.; resources, Z.L., H.Z. and G.M.; data curation, Z.L; writing—original draft preparation, Z.L.; writing—review and editing, Z.L., H.Z., G.M. and C.C.; visualization, Z.L. and G.M.; supervision, H.Z. and G.M.; project administration, H.Z.; funding acquisition, H.Z. All authors have read and agreed to the published version of the manuscript.

Funding: This research received the financially supported by the National Key R&D Program of China (Grant Nos. 2019YFE0112600), the National Natural Science Foundation of China (Grant Nos. 52078459), and the Natural Science Foundation of Zhejiang Province (Grant Nos. LZ22E080005).

Institutional Review Board Statement: Not applicable.

Informed Consent Statement: Not applicable.

Data Availability Statement: Not applicable.

Acknowledgments: The authors of this paper is very grateful to Wen-Cheng Liao of National Taiwan University for providing the experimental data of the concerned shear walls, and in the process of writing papers to provide valuable advice and suggestions.

Conflicts of Interest: The authors declare no conflict of interest.

References

1. Zhang, H.; Zhang, Y.; Lu, X.; Duan, Y.; Zhang, H. Influence of Axial Load Ratio on the Seismic Behavior of Steel Fiber–Reinforced Concrete Composite Shear Walls. *J. Struct. Eng.* **2020**, *146*, 04019171. [CrossRef]
2. Alarcon, C.; Hube, M.; de la Llera, J. Effect of axial loads in the seismic behavior of reinforced concrete walls with unconfined wall boundaries. *Eng. Struct.* **2014**, *73*, 13–23. [CrossRef]
3. Su, R.; Wong, S. Seismic behaviour of slender reinforced concrete shear walls under high axial load ratio. *Eng. Struct.* **2007**, *29*, 1957–1965. [CrossRef]
4. Li, X.; Zhang, J.; Cao, W. Hysteretic behavior of high-strength concrete shear walls with high-strength steel bars: Experimental study and modelling. *Eng. Struct.* **2020**, *214*, 110600. [CrossRef]
5. Lu, X.; Zhang, Y.; Zhang, H.; Zhang, H.; Xiao, R. Experimental study on seismic performance of steel fiber reinforced high strength concrete composite shear walls with different steel fiber volume fractions. *Eng. Struct.* **2018**, *171*, 247–259. [CrossRef]
6. Hosseini, S.A.; Kheyroddin, A.; Mastali, M. An experimental investigation into the impacts of eccentric openings on the in-plane behavior of squat RC shear walls. *Eng. Struct.* **2019**, *197*, 109410. [CrossRef]
7. Fattuhi, N.I. Strength of Sfrc Corbels Subjected to Vertical Load. *J. Struct. Eng. Asce* **1990**, *116*, 701–718. [CrossRef]
8. Thomas, J.; Ramaswamy, A. Mechanical Properties of Steel Fiber-Reinforced Concrete. *J. Mater. Civ. Eng.* **2007**, *19*, 385–392. [CrossRef]
9. Jayanth, K.; Prakash, M.N.S.; Suresh, G.S.; Naveen, B.O. Studies on the behaviour of steel fibre-reinforced concrete under monotonic and repeated cyclic stress in compression. *Arch. Civ. Mech. Eng.* **2022**, *22*, 50. [CrossRef]
10. Shi, X.; Park, P.; Rew, Y.; Huang, K.; Sim, C. Constitutive behaviors of steel fiber reinforced concrete under uniaxial compression and tension. *Constr. Build. Mater.* **2020**, *233*, 117316. [CrossRef]

11. Zhang, H.; Liu, X.; Yi, W. Experimental Investigation on Stress Redistribution and Load-Transfer Paths of Shear Walls with Openings. *J. Struct. Eng.* **2018**, *144*, 04018149. [CrossRef]
12. Popescu, C.; Sas, G.; Sabău, C.; Blanksvärd, T. Effect of Cut-Out Openings on the Axial Strength of Concrete Walls. *J. Struct. Eng.* **2016**, *142*, 04016100. [CrossRef]
13. Massone, L.M.; Muñoz, G.; Rojas, F. Experimental and numerical cyclic response of RC walls with openings. *Eng. Struct.* **2019**, *178*, 318–330. [CrossRef]
14. Wang, J.; Sakashita, M.; Kono, S.; Tanaka, H. Shear behaviour of reinforced concrete structural walls with eccentric openings under cyclic loading: Experimental study. *Struct. Des. Tall Spec. Build.* **2012**, *21*, 669–681. [CrossRef]
15. Dashti, F.; Dhakal, R.P.; Pampanin, S. Validation of a Numerical Model for Prediction of Out-of-Plane Instability in Ductile Structural Walls under Concentric In-Plane Cyclic Loading. *J. Struct. Eng.* **2018**, *144*, 04018039. [CrossRef]
16. Huang, C.-Y. The Study on Strength Prediction Model and Behavior of High Strength Steel Fiber Reinforced Concrete Walls with Opening. Master's Thesis, Department of Civil Engineering College of Engineering, National Taiwan University, Taipei, Taiwan, 2022. Available online: https://drive.google.com/file/d/1wpbOPdxmzh0RWemd0QkI21TI6X7JLayG/view?usp=sharing (accessed on 10 August 2022).
17. Ma, J.; Ning, C.-L.; Li, B. Peak Shear Strength of Flanged Reinforced Concrete Squat Walls. *J. Struct. Eng.* **2020**, *146*, 04020037. [CrossRef]
18. Wei, F.; Chen, H.; Xie, Y. Experimental study on seismic behavior of reinforced concrete shear walls with low shear span ratio. *J. Build. Eng.* **2022**, *45*, 103602. [CrossRef]
19. Fatemi, H.; Paultre, P.; Lamarche, C.-P. Evaluation of Inelastic Higher-Mode Effects on the Seismic Behavior of RC Structural Walls. *J. Struct. Eng.* **2020**, *146*, 04020016. [CrossRef]
20. Alwashali, H.; Maeda, M.; Ogata, Y.; Aizawa, N.; Tsurugai, K. Residual seismic performance of damaged reinforced concrete walls. *Eng. Struct.* **2021**, *243*, 112673. [CrossRef]
21. Rong, X.-L.; Zheng, S.-S.; Zhang, Y.-X.; Zhang, X.-Y.; Dong, L.-G. Experimental study on the seismic behavior of RC shear walls after freeze-thaw damage. *Eng. Struct.* **2020**, *206*, 110101. [CrossRef]
22. Erbaş, Y.; Anıl, Ö.; Özdemir, A.; Kopraman, Y. Prediction of capacity of reinforced concrete shear wall with multiple openings by using nonlinear finite element analysis. *Struct. Concr.* 2022; *Early view*. [CrossRef]
23. Kim, S.-H.; Lee, E.-K.; Kang, S.-M.; Park, H.-G.; Park, J.-H. Effect of boundary confinement on ductility of RC walls. *Eng. Struct.* **2021**, *230*, 111695. [CrossRef]
24. Zhang, Y.; Yuan, G.; Shu, Q.; Zhu, M.; Lu, L. Investigation on seismic behavior of RC shear walls with multiple post-construction openings based on experiment and simulation. *J. Build. Eng.* **2022**, *46*, 103707. [CrossRef]
25. Yang, C.; Chou, Y.-C.; Hung, C.-C. Seismic behavior of full-scale wall piers with high-strength steel reinforcement. *Eng. Struct.* **2022**, *256*, 114068. [CrossRef]
26. Barbachyn, S.M.; Devine, R.D.; Thrall, A.P.; Kurama, Y.C. Behavior of Nuclear RC Shear Walls Designed for Similar Lateral Strengths Using Normal-Strength versus High-Strength Materials. *J. Struct. Eng.* **2020**, *146*, 04020252. [CrossRef]
27. Hung, C.-C.; Hsieh, P.-L. Comparative study on shear failure behavior of squat high-strength steel reinforced concrete shear walls with various high-strength concrete materials. *Structures* **2020**, *23*, 56–68. [CrossRef]
28. Zhang, J.; Liu, J.; Li, X.; Cao, W. Seismic behavior of steel fiber-reinforced high-strength concrete mid-rise shear walls with high-strength steel rebar. *J. Build. Eng.* **2021**, *42*, 102462. [CrossRef]
29. Zhao, J.; Dun, H. A restoring force model for steel fiber reinforced concrete shear walls. *Eng. Struct.* **2014**, *75*, 469–476. [CrossRef]
30. Li, X.; Zhang, J.; Cao, W.; Zhu, Y. Seismic behavior of steel fiber reinforced high strength concrete shear walls with different embedded steel configurations. *J. Build. Eng.* **2022**, *53*, 104551. [CrossRef]
31. Sakr, M.A.; El-Khoriby, S.R.; Khalifa, T.M.; Nagib, M.T. Modeling of RC shear walls strengthened with ultra-high performance fiber reinforced concrete (UHPFRC) jackets. *Eng. Struct.* **2019**, *200*, 109696. [CrossRef]
32. Nagib, M.T.; Sakr, M.A.; El-Khoriby, S.R.; Khalifa, T.M. Cyclic behaviour of squat reinforced concrete shear walls strengthened with ultra-high performance fiber reinforced concrete. *Eng. Struct.* **2021**, *246*, 112999. [CrossRef]
33. Hung, C.-C.; Li, H.; Chen, H.-C. High-strength steel reinforced squat UHPFRC shear walls: Cyclic behavior and design implications. *Eng. Struct.* **2017**, *141*, 59–74. [CrossRef]
34. Kassem, W.; Elsheikh, A. Estimation of Shear Strength of Structural Shear Walls. *J. Struct. Eng.* **2010**, *136*, 1215–1224. [CrossRef]
35. Zhang, H.; Fang, Y.; Duan, Y.; Du, G. The V-MVLE model for cyclic failure behavior simulation of planar RC members. *Thin-Walled Struct.* **2022**, *181*, 110159. [CrossRef]
36. Abdullah, S.A.; Wallace, J.W. Drift Capacity at Axial Failure of RC Structural Walls and Wall Piers. *J. Struct. Eng.* **2021**, *147*, 04021062. [CrossRef]
37. Li, B.; Chi, Y.; Xu, L.; Li, C.; Shi, Y. Cyclic tensile behavior of SFRC: Experimental research and analytical model. *Constr. Build. Mater.* **2018**, *190*, 1236–1250. [CrossRef]
38. Lee, S.C.; Oh, J.H.; Cho, J.Y. Compressive Behavior of Fiber-Reinforced Concrete with End-Hooked Steel Fibers. *Materials* **2015**, *8*, 1442–1458. [CrossRef]
39. Wang, X.; Fan, F.; Lai, J.; Xie, Y. Steel fiber reinforced concrete: A review of its material properties and usage in tunnel lining. *Structures* **2021**, *34*, 1080–1098. [CrossRef]

40. Kytinou, V.K.; Chalioris, C.E.; Karayannis, C.G.; Elenas, A. Effect of Steel Fibers on the Hysteretic Performance of Concrete Beams with Steel Reinforcement-Tests and Analysis. *Materials* **2020**, *13*, 2923. [CrossRef]
41. Ravichandran, D.; Prem, P.R.; Kaliyavaradhan, S.K.; Ambily, P. Influence of fibers on fresh and hardened properties of Ultra High Performance Concrete (UHPC)—A review. *J. Build. Eng.* **2022**, *57*, 104922. [CrossRef]
42. Li, B.; Prem, P.R.; Kaliyavaradhan, S.K.; Ambily, P. Experimental investigation on the stress-strain behavior of steel fiber reinforced concrete subjected to uniaxial cyclic compression. *Constr. Build. Mater.* **2017**, *140*, 109–118. [CrossRef]
43. Deng, F.; Chi, Y.; Xu, L.; Huang, L.; Hu, X. Constitutive behavior of hybrid fiber reinforced concrete subject to uniaxial cyclic tension: Experimental study and analytical modeling. *Constr. Build. Mater.* **2021**, *295*, 123650. [CrossRef]
44. dos Santos, L.R.; de Sousa Cardoso, H.; Caldas, R.B.; Grilo, L.F. Finite element model for bolted shear connectors in concrete-filled steel tubular columns. *Eng. Struct.* **2020**, *203*, 109863. [CrossRef]
45. Li, W.; Han, L.-H. Seismic performance of CFST column to steel beam joints with RC slab: Analysis. *J. Constr. Steel Res.* **2011**, *67*, 127–139. [CrossRef]
46. Fang, C.; Ali, M.S.M.; Sheikh, A.H.; Singh, M. Numerical and Finite-Element Analysis of Short Ultrahigh-Performance Fiber-Reinforced Concrete Columns. *J. Struct. Eng.* **2019**, *145*, 04019111. [CrossRef]
47. Cai, J.; Pan, J.; Tan, J.; Vandevyvere, B. Nonlinear finite-element analysis for hysteretic behavior of ECC-encased CFST columns. *Structures* **2020**, *25*, 670–682. [CrossRef]
48. Bonilla, J.; Bezerra, L.M.; Mirambell, E. Resistance of stud shear connectors in composite beams using profiled steel sheeting. *Eng. Struct.* **2019**, *187*, 478–489. [CrossRef]
49. Abouali, S.; Shahverdi, M.; Ghassemieh, M.; Motavalli, M. Nonlinear simulation of reinforced concrete beams retrofitted by near-surface mounted iron-based shape memory alloys. *Eng. Struct.* **2019**, *187*, 133–148. [CrossRef]
50. Raza, A.; Khan, Q.u.Z.; Ahmad, A. Investigation of HFRC columns reinforced with GFRP bars and spirals under concentric and eccentric loadings. *Eng. Struct.* **2021**, *227*, 111461. [CrossRef]
51. Paulay, T.; Priestly, M.J.N. *Seismic Design of Reinforced Concrete and Masonry Buildings*, 1st ed.; John Wiley & Sons, Inc.: New York, NY, USA, 1992.
52. Zhang, H.Y.; Cheng, X.; Li, Y.; Du, X. Prediction of failure modes, strength, and deformation capacity of RC shear walls through machine learning. *J. Build. Eng.* **2022**, *50*, 104145. [CrossRef]